Supplementary Information for

Versatile biological imaging enabled by multimodal fluorescence-phase microscopy

Wenshu Wang[1, †], Suyi Zhong[1, †], Ruijie Cao[1, †], Xiaoyu Bu[2], Shu Gao[1], Qianxi Liang[1], Yunzhe Fu[1], Xuantao Su[3], Meiqi Li[4, *], and Peng Xi[1, *]

[1] Department of Biomedical Engineering, National Biomedical Imaging Center, College of Future Technology, Peking University, Beijing, 100871, China

[2] Key Laboratory of Analytical Science and Technology of Hebei Province, College of Chemistry and Material Science, Hebei University, Baoding, 071002, China

[3] School of Integrated Circuits, Shandong University, Jinan, 250101, China

[4] School of Life Sciences, Peking University, Beijing, 100871, China

† Equal Contribution.

*limeiqi@pku.edu.cn

*xipeng@pku.edu.cn

Contents

Supplementary Note 1: Phase reconstruction algorithm for DPC imaging 1

Supplementary Note 2: Background-removed super-resolution reconstruction with frame-reduced strategies and polarization resolution 4

Supplementary Note 3: Timing control of MFPM 8

Supplementary Note 4: Imaging speed validation and field of view of MFPM 10

Supplementary Note 5: Evaluation of the frame-reduction algorithm 12

Supplementary Note 6: Core parameter selection strategy 16
    6.1 LED-array configuration 16
    6.2 The regularization parameter in phase reconstruction 18
    6.3 Cutoff frequency and filtering window size of Dark Sectioning 18

Supplementary Note 7: Multimodal imaging of mouse skin tissue sections 21

Supplementary Note 8: MFPM imaging of cell death dynamics 23

Supplementary Note 9: Sample Preparation 25
    9.1 Preparation of fluorescent beads samples 25
    9.2 Preparation of zebrafish samples 25

Supplementary Tables 26

Supplementary Figures 27

Reference 28

Supplementary Note 1: Phase reconstruction algorithm for DPC imaging

In the phase retrieval process, the complex transmission function $t_s(\boldsymbol{r})$ of a thin sample can be expressed as $t_s(\boldsymbol{r}) = \exp\left[-\mu_s(\boldsymbol{r}) + i\varphi_s(\boldsymbol{r})\right]$, where $\boldsymbol{r}$ denotes the spatial coordinates of the sample, μ_s and φ_s represents the absorption and phase-related properties of the sample, respectively. Under the weak scattering approximation, the higher-order terms in μ_s and φ_s can be neglected, leading to a linear approximation of the sample's transmission function[1], expressed as $t_s(\boldsymbol{r}) \approx 1 - \mu_s(\boldsymbol{r}) + i\varphi_s(\boldsymbol{r})$, thereby enabling the separation of the sample's absorption term and phase term. The sample is illuminated by a uniformly distributed plane wave incident at a tilt angle $S(\boldsymbol{u'})$, where $\boldsymbol{u'}$ denotes the spatial frequency vector of the tilted illumination. Subsequently, the transmitted wave-front passes through the pupil function $P(\boldsymbol{u})$ of the objective lens, and the intensity distribution on the camera plane can be obtained. The intensity's spectrum $\mathcal{F}\{I(\boldsymbol{u})\}$ can be decomposed into three components: the background term, the absorption-related term, and the phase-related term:

$$\begin{aligned} \mathcal{F}\{I(\boldsymbol{u})\} &= S(\boldsymbol{u'})\delta(\boldsymbol{u})\,|P(\boldsymbol{u'})|^2 \\ &\quad - S(\boldsymbol{u'})\mathcal{F}\{\mu_s(\boldsymbol{u})\}[P^*(\boldsymbol{u'})P(\boldsymbol{u}+\boldsymbol{u'}) + P(\boldsymbol{u'})P^*(\boldsymbol{u}-\boldsymbol{u'})] \\ &\quad + iS(\boldsymbol{u'})\mathcal{F}\{\varphi_s(\boldsymbol{u})\}[P^*(\boldsymbol{u'})P(\boldsymbol{u}+\boldsymbol{u'}) + P(\boldsymbol{u'})P^*(\boldsymbol{u}-\boldsymbol{u'})] \\ &= B_{LED}\delta(\boldsymbol{u}) + H_{abs}(\boldsymbol{u})\cdot\mathcal{F}\{\mu_s(\boldsymbol{u})\} + H_{pha}(\boldsymbol{u})\cdot\mathcal{F}\{\varphi_s(\boldsymbol{u})\} \end{aligned} \tag{1}$$

where B_{LED} represents the total energy passing through the imaging system, H_{abs} and H_{pha} are the amplitude transfer function and the phase transfer function respectively, * is the conjugate symbol, and $\mathcal{F}\{\bullet\}$ corresponds to the Fourier transformation.

In differential phase contrast (DPC) imaging, raw data is captured using asymmetric illumination patterns produced by a programmable LED array. Specifically, two DPC reconstructions are proposed in this study: Fast DPC (fDPC), which rapidly obtain the phase gradient by normalized differential processing using only two raw images, and quantitative DPC (qDPC), which recovers quantitative phase information through deconvolution.

When employing semi-circular or semi-ring illumination, the measured intensities from the two complementary modes are acquired (e.g., $I_U(\boldsymbol{r}_c)$ and $I_D(\boldsymbol{r}_c)$, which represent the images captured under up and down illumination directions). The bright-field (BF) image can then be derived by computing the average of these two intensity measurements:

$$I_{BF}(\boldsymbol{r}_c) = (I_U(\boldsymbol{r}_c) + I_D(\boldsymbol{r}_c))/2 \tag{2}$$

where $\boldsymbol{r}_c$ represents the coordinates on the camera plane. Then the fDPC imaging can be derived by differential normalization and expressed as:

$$I_{\mathrm{DPC}}(\boldsymbol{r}_c)=\frac{I_U(\boldsymbol{r}_c)-I_D(\boldsymbol{r}_c)}{I_U(\boldsymbol{r}_c)+I_D(\boldsymbol{r}_c)} \tag{3}$$

Equation (3) leverages the symmetry between the up and down halves of the pupil function to effectively cancel out the background term, thereby enhancing the phase contrast in the resulting image. In the absence of aberrations, the pupil function of the objective lens can be modeled as a circular, real and centrosymmetric aperture, with a radius determined by the numerical aperture (NA) of the objective. Based on this principle, the Fourier spectrum of the raw image can be expressed as:

$$\begin{aligned}\mathcal{F}\{I(\boldsymbol{u})\}&=H(\boldsymbol{u})\cdot\mathcal{F}\{\varphi_s(\boldsymbol{u})\}\\&=\frac{\iint S_{UD}(\boldsymbol{u}')\left[P^*(\boldsymbol{u}')P(\boldsymbol{u}+\boldsymbol{u}')-P(\boldsymbol{u}')P^*(\boldsymbol{u}-\boldsymbol{u}')\right]d^2\boldsymbol{u}'}{\iint\left|S_{UD}(\boldsymbol{u}')\right|\left|P(\boldsymbol{u}')\right|^2d^2\boldsymbol{u}'}\mathcal{F}\{\varphi_s(\boldsymbol{u})\}\\&=\frac{H_{pha}(\boldsymbol{u})}{B_{LED}}\mathcal{F}\{\varphi_s(\boldsymbol{u})\}\end{aligned} \tag{4}$$

here, $S_{UD}(\boldsymbol{u}')$ represents the distribution of light sources by dividing the LEDs into up and down illumination directions and B_{LED} can be approximated by averaging the two images acquired under asymmetric illumination conditions. As indicated in Equation (4), the quantitative phase values can be analytically retrieved by solving the inverse problem in conjunction with the phase transfer function, typically achieved by deconvolving the raw image with $H(\boldsymbol{u})$.

However, the phase transfer function generally exhibits zero values along the asymmetric complementary illumination source division direction and outside the passband, which leads to information loss in certain directions and numerical singularities if deconvolution is performed directly. To address this, multiple sets of raw images acquired under different illumination directions can be combined, and the Tikhonov regularization is introduced to stabilize the solution and suppress noise amplification. The optimal sample phase function spectrum $\mathcal{F}\{\varphi_{\mathrm{s}}(\boldsymbol{u})\}^*$ can be obtained by solving the following optimization problem:

$$\underset{\mathcal{F}\{\varphi_{\mathrm{s}}\}}{\arg\min}\sum_j\left|\mathcal{F}\{I_j(\boldsymbol{u})\}-H_j(\boldsymbol{u})\cdot\mathcal{F}\{\varphi_{\mathrm{s}}(\boldsymbol{u})\}\right|^2+\alpha_{\mathrm{DPC}}\left|\mathcal{F}\{\varphi_{\mathrm{s}}(\boldsymbol{u})\}\right|^2 \tag{5}$$

here, j denotes the number of raw image pairs used for quantitative phase reconstruction. α_{DPC} is the regularization parameter. The quantitative phase is obtained by setting the gradient of the objective function to zero:

$$\varphi_s(\boldsymbol{r}) = F^{-1}\left\{\frac{\sum_j \left[H_j^*(\boldsymbol{u})\cdot F\left\{I_j(\boldsymbol{u})\right\}\right]}{\sum_j \left|H_j(\boldsymbol{u})\right|^2+\alpha_{\mathrm{DPC}}}\right\} \tag{6}$$

where $F^{-1}\{\cdot\}$ represents the inverse Fourier transform. The specific algorithm flow chart is shown in Fig. S1.

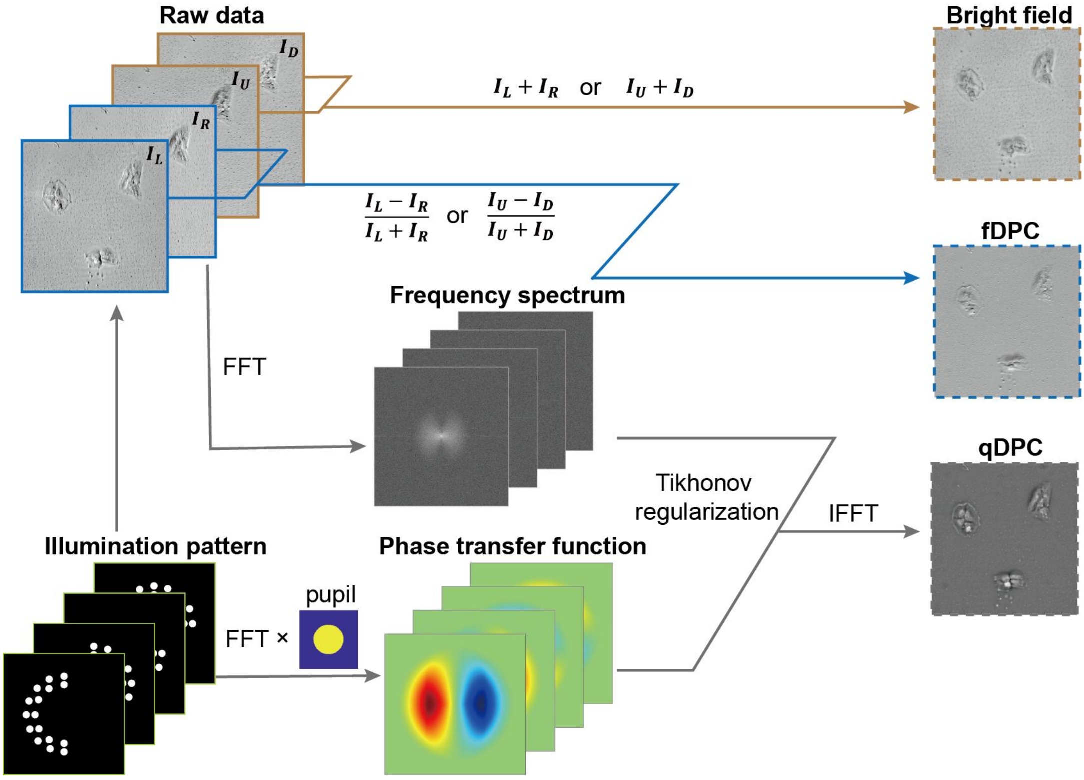

Fig. S1 DPC imaging algorithm flow chart. Images I_U, I_D, I_L, and I_R depict intensity images illuminated sequentially from up, down, left, and right directions, respectively.

Supplementary Note 2: Background-removed super-resolution reconstruction with frame-reduced strategies and polarization resolution

During fluorescence image reconstruction, the dark channel optical sectioning algorithm can be employed to effectively distinguish in-focus information from defocused background, thereby enabling background removal. In this algorithm, it is assumed that the dark channel value is zero in in-focus regions and non-zero in defocused areas. Since the defocused background predominantly exists in the low-frequency components $Lo(D_{\theta,\varphi}(\boldsymbol{r}))$ of the acquired image spectrum, whereas the high-frequency components $Hi(D_{\theta,\varphi}(\boldsymbol{r}))$ contains modulated information from structured illumination. $Hi[\cdot]$ and $Lo[\cdot]$ are high-pass filter and low-pass filter, and $D_{\theta,\varphi}(\boldsymbol{r})$ is the fluorescence signal received by the camera, with θ denoting the illumination direction and φ denoting the phase. To preserve the weak signals embedded in the high-frequency domain, dark channel processing is applied only to the $Lo(D_{\theta,\varphi}(\boldsymbol{r}))$ component. The low-pass filtered image $Lo(D_{\theta,\varphi}(\boldsymbol{r}))$ is decomposed into background-free components $J(\boldsymbol{r})$ and background components $B(\boldsymbol{r})$. According to the dark channel prior, the in-focus region satisfied $Dark\{J(\boldsymbol{r})\}=0$, where $Dark[\cdot]$ denotes the dark channel operation. By defining the proportion of $J(\boldsymbol{r})$ in the image as the transmission coefficient $T_{\mathrm{J}}(\boldsymbol{r})$, $Lo(D_{\theta,\varphi}(\boldsymbol{r}))$ can be expressed as:

$$Lo(D_{\theta,\varphi}(\boldsymbol{r})) = T_{\mathrm{J}}(\boldsymbol{r})\cdot J(\boldsymbol{r}) + (1-T_{\mathrm{J}}(\boldsymbol{r}))\cdot B(\boldsymbol{r}) \tag{7}$$

Since $B(\boldsymbol{r})$ remains a part of the low-frequency components within $Lo(D_{\theta,\varphi}(\boldsymbol{r}))$, a low-pass filter with a lower cutoff frequency $EL[\cdot]$ is applied to the original fluorescence image. Then we can get $B(\boldsymbol{r}) \approx EL(D_{\theta,\varphi}(\boldsymbol{r}))$. Assuming that $T_{\mathrm{J}}(\boldsymbol{r})$ remains approximately constant within each image patch, the dark channel operation can be applied to both sides of Equation (7), yielding:

$$Dark\left\{\frac{Lo(D_{\theta,\varphi}(\boldsymbol{r}))}{EL(D_{\theta,\varphi}(\boldsymbol{r}))}\right\} = T_{\mathrm{J}}(\boldsymbol{r})\cdot Dark\left\{\frac{J(\boldsymbol{r})}{EL(D_{\theta\varphi}(\boldsymbol{r}))}\right\} + 1 - T_{\mathrm{J}}(\boldsymbol{r}) \tag{8}$$

Considering that $Dark\{J(\boldsymbol{r})\}=0$, we can assume $Dark\{J(\boldsymbol{r})/EL(D_{\theta,\varphi}(\boldsymbol{r}))\}=0$, and correspondingly we can get $T_{\mathrm{J}}(\boldsymbol{r})$:

$$T_{\mathrm{J}}(\boldsymbol{r}) = 1 - Dark\left\{\frac{Lo(D_{\theta,\varphi}(\boldsymbol{r}))}{EL(D_{\theta,\varphi}(\boldsymbol{r}))}\right\} \tag{9}$$

Combining $T_{\mathrm{J}}(\boldsymbol{r})$ obtained by Equation (9) and the estimated background part $B(\boldsymbol{r})$, we can substitute it into Equation (7) to obtain the background-free part $J(\boldsymbol{r})$ of $Lo(D_{\theta,\varphi}(\boldsymbol{r}))$:

$$J(\boldsymbol{r})=\frac{Lo(D_{\theta,\varphi}(\boldsymbol{r}))-(1-T_{\mathrm{J}}(\boldsymbol{r}))\cdot B(\boldsymbol{r})}{T_{\mathrm{J}}(\boldsymbol{r})} \tag{10}$$

In the process of defocused background removal using the dark channel method, $Lo(D_{\theta,\varphi}(\boldsymbol{r}))$ and $Hi(D_{\theta,\varphi}(\boldsymbol{r}))$ are typically divided based on a predefined threshold, which is often chosen as $f_{\mathrm{OTF}}/2$ to minimize the influence of illumination modulation peaks in the frequency domain, where f_{OTF} means the cutoff frequency of the optical transfer function (OTF). The component $T_{\mathrm{J}}(\boldsymbol{r})$ is obtained through minimum filtering operation, where each pixel is replaced by the minimum value within its local neighborhood. The size of the filtering window is determined according to the point spread function (PSF) of the imaging system.

Conventional structured illumination microscopy (SIM) requires 9 raw images modulated by structured illumination patterns, covering 3 illumination directions with 3 phase shifts per direction (phase difference is $\pi/3$). The spectrum is then separated and shifted in the frequency domain to complete the reconstruction. In this work, a frame-reduction reconstruction technique based on the least-squares method is adopted, allowing super-resolution reconstruction from only 6 images: 3 illumination directions with 2 phase shifts per direction (phase difference is π). Since the subsequent polarization analysis is performed using wide-field (WF) images, the polarization response is not considered during the structured illumination-based super-resolution reconstruction process. During the structured illumination imaging process, the ±1 diffraction orders from the digital micromirror device (DMD) are configured to interfere coherently at the sample $S(\boldsymbol{r})$. The resulting structured light pattern is characterized by an illumination angle θ and φ, and the corresponding two-dimensional structured illumination field in the spatial domain can be expressed as:

$$I_{\theta,\varphi}(\boldsymbol{r})=I_0\left[1+m\cos(\boldsymbol{k}_\theta\cdot\boldsymbol{r}+\varphi)\right] \tag{11}$$

where m is the modulation factor of the structured illumination fringes, and $\boldsymbol{k}_\theta$ represents the spatial frequency of the illumination pattern at the illumination angle θ. Accordingly, the fluorescence signal emitted from the sample and recorded by the camera can be expressed as:

$$D_{\theta,\varphi}(\boldsymbol{r})=\left[S(\boldsymbol{r})\cdot I_{\theta,\varphi}(\boldsymbol{r})\right]\otimes h(\boldsymbol{r})+b(\boldsymbol{r}) \tag{12}$$

where $h(\boldsymbol{r})$ denotes the PSF of the system, and $b(\boldsymbol{r})$ represents the defocused background component. Since the 2D structured illumination is based on WF detection and only involves lateral modulation, defocused background from planes above and below the focal plane is also captured during signal acquisition.

Therefore, the optical sectioned signal with background removed $D'_{\theta,\varphi}(\boldsymbol{r})$ can be denoted as:

$$\begin{aligned} D'_{\theta,\varphi}(\boldsymbol{r}) &= Hi(D_{\theta,\varphi}(\boldsymbol{r})) + Dark\left\{Lo(D_{\theta,\varphi}(\boldsymbol{r}))\right\} \\ &= \left[S(\boldsymbol{r})\cdot I_{\theta,\varphi}(\boldsymbol{r})\right]\otimes h(\boldsymbol{r}) \end{aligned} \tag{13}$$

By applying Fourier transform to both sides of Equation (13), the background-free frequency-domain signal $D'_{\theta,\varphi}(\boldsymbol{k})$ can be described as the convolution of the sample's spatial frequency distribution $S(\boldsymbol{k})$ and the intensity distribution of the structured illumination pattern $I_{\theta,\varphi}(\boldsymbol{k})$, multiplied by the system's OTF $h(\boldsymbol{k})$. The OTF has a cutoff frequency denoted as K_{OTF}, and the result is expressed as:

$$D'_{\theta,\varphi}(\boldsymbol{k}) = \left[S(\boldsymbol{k})\otimes I_{\theta,\varphi}(\boldsymbol{k})\right]\cdot h(\boldsymbol{k}) \tag{14}$$

Substituting the Fourier transformation of Equation (11) into Equation (14), combined with the cosine function to expand into a complex exponential form, its corresponding Fourier transform is an impulse function, and the $D'_{\theta,\varphi}(\boldsymbol{k})$ can be expressed as the following form:

$$D'_{\theta,\varphi}(\boldsymbol{k}) = I_0\cdot\left(S(\boldsymbol{k}) + \exp(-i\varphi)S(\boldsymbol{k}+\boldsymbol{k}_\theta)/2 + \exp(i\varphi)S(\boldsymbol{k}-\boldsymbol{k}_\theta)/2\right)\cdot h(\boldsymbol{k}) \tag{15}$$

Combined with the frequency domain diagram in the middle of Fig. 2a, it can be seen that when $|\boldsymbol{k}| < K_{\mathrm{OTF}}$, each pixel in $D'_{\theta,\varphi}(\boldsymbol{k})$ is the result of the linear superposition of the three pixel values in $S(\boldsymbol{k})$. Therefore, each pixel in $D'_{\theta,\varphi}(\boldsymbol{k})$ are represented by the one-dimensional set of $\boldsymbol{d}'_{\theta,\varphi}$, and Equation (15) can be converted into a matrix expression:

$$\boldsymbol{d}'_{\theta,\varphi} = \boldsymbol{M}_{\theta,\varphi}\cdot\boldsymbol{S}_\theta \tag{16}$$

where $\boldsymbol{M}_{\theta,\varphi}$ denotes the result of multiplying the pixel in the system OTF with the three modulation points, and $\boldsymbol{S}_\theta$ corresponds to the selected pixel group from the sample's frequency spectrum $S(\boldsymbol{k})$. By concatenating the frequency-domain distributions under all illumination angles θ and φ, the frequency domain expression of the structured light modulation process can be obtained as follows:

$$\boldsymbol{d}' = \boldsymbol{M}\cdot\boldsymbol{S} \tag{17}$$

where $\boldsymbol{d}'$ is the combination of the known original image frequency domain $D'_{\theta,\varphi}(\boldsymbol{k})$, $\boldsymbol{M}$ is the combination of the known system OTF and the illumination stripe multiplication result (the matrix size is $length(\boldsymbol{d}')\times length(\boldsymbol{S})$, and $length[\cdot]$ is the matrix size), and $\boldsymbol{S}$ is the set of the super-resolution image to be obtained. Subsequently, the cross-correlation methods[2, 3] implemented in the open-source reconstruction framework is employed to extract the frequency, phase, and orientation of the structured illumination patterns from the raw images. These parameters are then used to reconstruct the illumination fringe field and incorporated as known quantities in the construction of matrix $\boldsymbol{M}$. Since the number of pixels in the original image is greater than the number of pixels in the super-resolution image, namely $length(\boldsymbol{d}') > length(\boldsymbol{S})$, the solution of the linear equations can be converted into the process of least-squares optimization, yielding the solution for $\boldsymbol{S}$ is:

$$\boldsymbol{S} = (\boldsymbol{M}^T \boldsymbol{M})^{-1} \boldsymbol{M}^T \boldsymbol{d}' \tag{18}$$

here, $\boldsymbol{M}^T$ denotes the transpose of matrix $\boldsymbol{M}$. The frequency domain of the final super-resolution image $S(\boldsymbol{k})$ can be obtained by reordering the elements of $\boldsymbol{S}$ according to the arranged pixel order.

After applying a Wiener filter-based optimization (denoted as *Optimizer*) to the spectrum of the reconstructed super-resolution image, an inverse Fourier transform is performed to obtain the final spatial-domain super-resolution result:

$$S(\boldsymbol{r}) = F^{-1}\left[S(\boldsymbol{k}) \cdot Optimizer\right] \tag{19}$$

Due to the large size of matrix $\boldsymbol{M}$, the input images are divided into 100 pixel × 100 pixel subregions and processed in blocks, which significantly enhances the computational efficiency of frame-reduced SIM reconstruction. For the selection of different parameters during reconstruction, see Supplementary Note 6.

Supplementary Note 3: Timing control of MFPM

In this study, the devices that should be synchronized are the LED array, DMD, and camera. Device's timing control is implemented via communication between a host PC and an Arduino microcontroller (Arduino Mega 2560). We use MATLAB to drive the communication and built a graphical user interface (GUI) with App Designer. The Arduino is pre-flashed with a command interpreter and remains in a standby state, waiting for commands from the host. A screenshot of the GUI is shown in Fig. S2a.

The GUI is divided into two main areas: the upper panel for entering basic acquisition parameters, and the lower panel for selecting acquisition modes. Mode selection in the lower panel allows flexible combinations of imaging modes without the need to re-flash the microcontroller for each timing configuration. This design avoids the limitation of fixed pulse-sequence outputs that would arise if timing were hard-coded on the microprogrammed control unit.

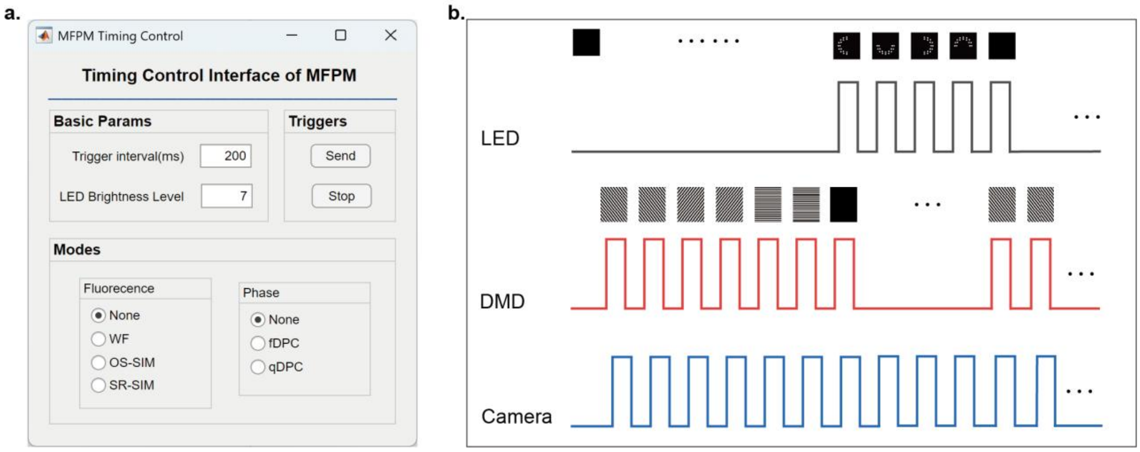

Timing Control Interface of MFPM

Basic Params

Trigger interval(ms) 200

LED Brightness Level 7

Triggers

Modes

Fluorecence
● None
○ WF
○ OS-SIM
○ SR-SIM

Phase
● None
○ fDPC
○ qDPC

Fig. S2. Timing control interface of MFPM and output examples. a. The GUI designed in MATLAB, which mainly contains basic parameters setting, imaging mode selection, and trigger signal output sections. b. Example of an output trigger when selecting SR-SIM and qDPC modes.

An example timing diagram is shown in Fig. S2b, corresponding to a combined acquisition of SR-SIM in the fluorescence module and qDPC in the phase module. In each cycle, the DMD first receives a trigger pulse, followed by the camera trigger pulses that capture the frames corresponding to different DMD patterns. For the SIM acquisition we require six trigger pulses. After the sixth camera trigger, the DMD emits one additional pattern trigger because our pattern set includes an extra "all-on" pattern. In that state the excitation laser is no longer diffracted by the DMD pattern and the beam is blocked by the physical mask, thereby effectively interrupting fluorescence excitation. Concurrently, the LED array executes its preconfigured illumination cycle;

the camera is synchronized to the LED timing and records the associated signals. Immediately before the next DMD cycle begins, the LED source is driven to an all-off state to prevent interference with the subsequent fluorescence acquisition. The arrangement of the DMD patterns used in this example are depicted in Fig. S2b.

This PC-driven, command-based architecture enables rapid reconfiguration of acquisition modes and flexible combinations of illumination and patterning sequences while keeping the microcontroller firmware simple and robust. Therefore, this configuration greatly facilitates the timing control and data acquisition of the MFPM system.

Furthermore, we ruled out the possibility of crosstalk between different devices. Specifically, the camera continuously captured 30 images under different operating conditions at the same exposure time. The statistical results are shown in Table S1 and Fig. S3. We found that even when the DMD electronics were powered on and triggered, there was no significant increase in readout noise or offset. This confirms that the electrical coupling of the DMD does not affect the fidelity of the DPC signal.

Table S1. Average pixel value of camera's baseline under different system states.

Number	LED	DMD	Camera	Baseline of camera (16 bit)
System State 1	OFF	OFF	ON	137.241
System State 2	ON	OFF	ON	137.134
System State 3	ON	ON	ON	137.200

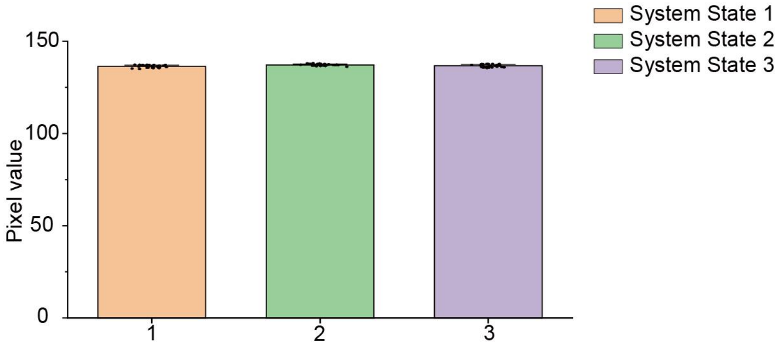

Fig. S3 The average pixel value of the camera baseline under different system states. 30 images were captured for each state.

Supplementary Note 4: Imaging speed validation and field of view of MFPM

For fluorescence excitation at 561 nm, the optical power measured at the sample plane was 93.7 µW. For the LED-array illumination used in fDPC and qDPC, the power was 24.9 µW, which was substantially lower than the laser excitation power and therefore didn't not introduce additional phototoxicity. However, because LEDs provide incoherent uniform illumination, their power density is much lower than that of two interfering laser beams, which makes them very cell-friendly.

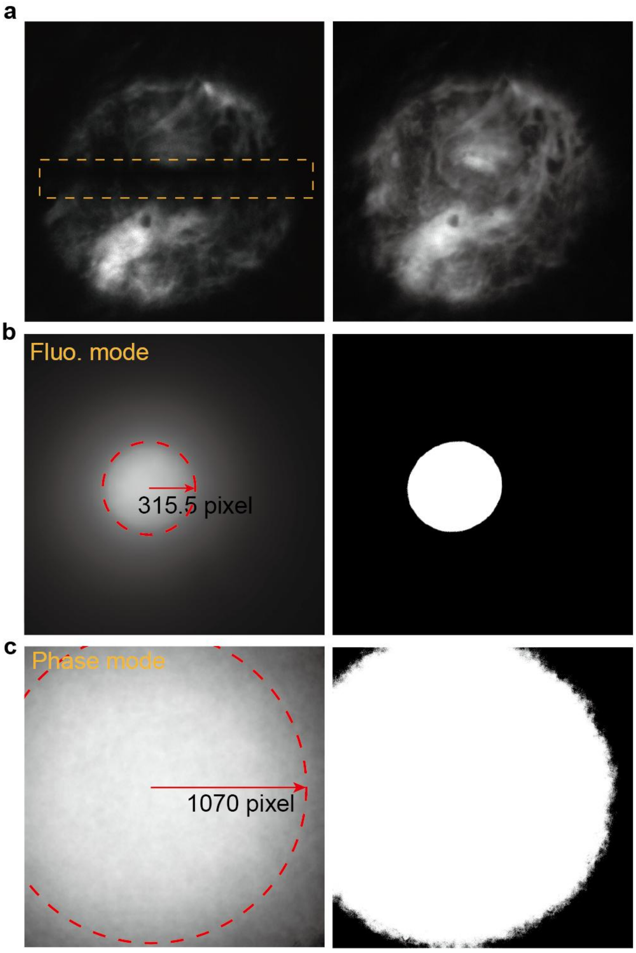

Fig.S4 Imaging speed validation and field of view of MFPM. a. Images captured at trigger intervals of less than 15ms (left image) and 15ms (right image) with a size of 736 pixel × 736 pixel. The orange rectangle indicates that several data was missing due to the rolling-shutter readout mechanism of the camera. b. Measured FOV and threshold segmentation results of fluorescence imaging. c. Measured FOV and threshold segmentation results of phase imaging.

About acquisition time, we experimentally evaluated the minimal safe trigger interval for stable acquisition. As described in response to Fig. S4, our experiments determined that when the trigger interval is less than 15 ms, due to the limited readout speed of the camera, the captured image will miss several data due to the rolling-shutter readout mechanism of the camera, as shown in the left part of Fig. S4a. Experimental testing showed that a trigger interval of 15 ms ensures clear readout of all modes. This corresponds to a full 10-frame multimodal cycle of about 150 ms. Thus, when the individual modes of fluorescence or phase were run independently, they can achieve higher throughput. It’s worth noting that the image size we tested was 736 pixel ×736 pixel, even faster processing speeds can be achieved by further reducing the size of images.

We also provided quantitative FOV measurements for the effective illumination region. To obtain the quantitative FOV, we imaged a uniform fluorescent plate for SIM and an unloaded glass slide for DPC conditions, followed by threshold segmentation to delineate the field boundary. The radius of the valid circular imaging region was then extracted from the segmented mask, as shown in Figs. S4b, c. Since we used the same camera (2048 pixel × 2048 pixel, 6.5 μm pixels) and configurations to capture data, we can use the number of pixels to characterize the relative size of the FOV. The fluorescence modality yielded a circular FOV of approximately 631 pixels in diameter, whereas the phase modality used nearly the full camera sensor and achieved an effective diameter of 2140 pixels. This confirms that the usable FOV of phase modality is more than times of fluorescence in terms of imaging area, and is consistent with the intended roles of the two modalities in high-resolution and large-field imaging, respectively.

Supplementary Note 5: Evaluation of the frame-reduction algorithm

To comprehensively evaluate the performance of our proposed 6-frame SIM (SIM6) in comparison with the conventional 9-frame SIM (SIM9), we conducted simulations on a variety of structures, including line-shaped, point-shaped, and circle-shaped features. The reconstructed images for both methods are systematically compared in Fig. S5a. Quantitative image decorrelation analysis, presented in Fig. S5b, demonstrate that both techniques provided a substantial resolution enhancement of approximately 1.82-fold relative to wide-field microscopy. In addition, qualitative and quantitative contrast evaluations indicated that the 6-frame and 9-frame SIM approaches achieve similar contrast performance, which is significantly superior to that of WF imaging. Importantly, both SIM modes are able to clearly resolve adjacent line structures that remained indistinguishable under conventional WF conditions, as shown in Fig. S5c, thereby unequivocally validating the resolution improvement afforded by structured illumination.

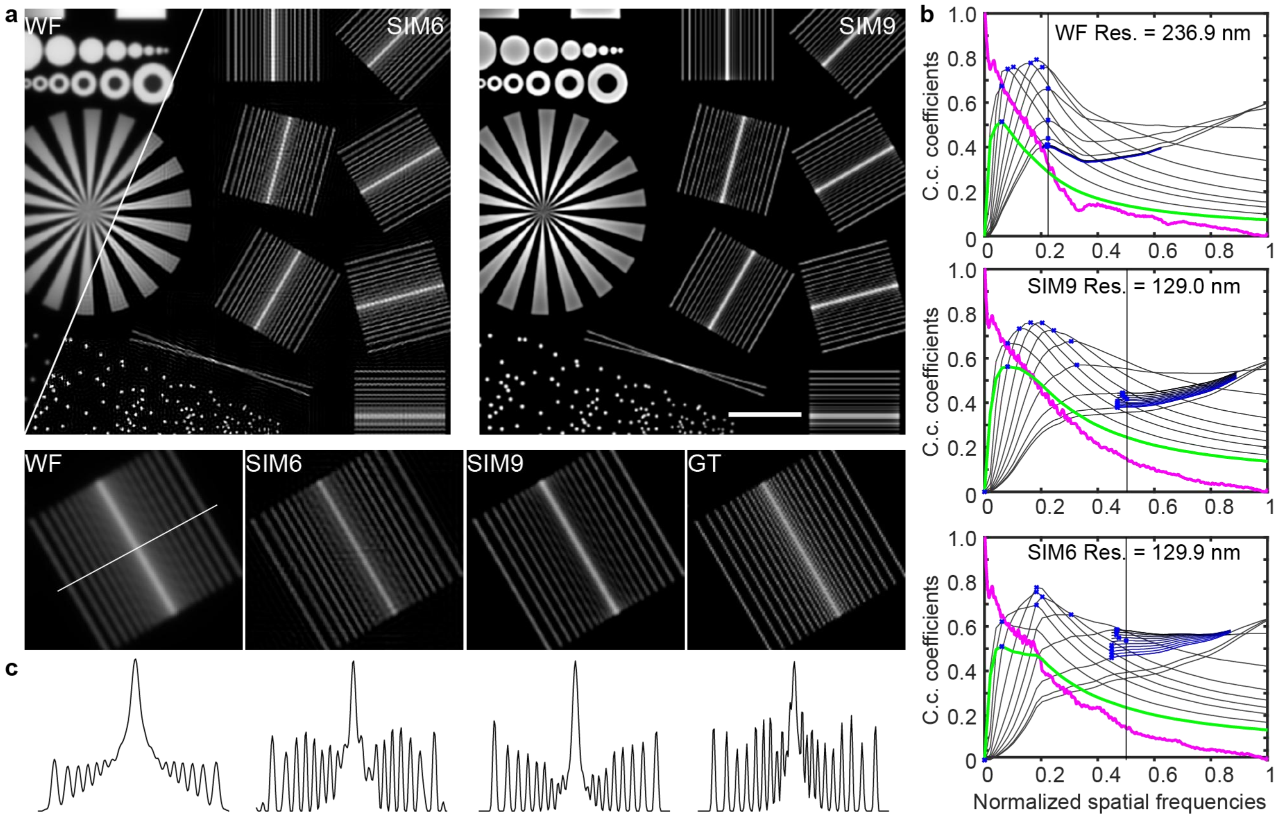

Fig. S5 Comparison of 9-frame and 6-frame SIM. a. WF and reconstructed SIM images of various kinds of simulation samples. b. Image decorrelation analysis of resolution. c. Grayscale profile of WF and SIM results extracted along the white line in a. Scale bar: 4 μm.

We further compared the performance of our frame-reduction SIM with conventional SIM9 on real samples of mitochondria and actin filaments. To acquire the images, we modified the timing of our MFPM system to capture 12 raw images, corresponding to three angles with four phases each: 0, 2π/3, π, and 4π/3. This allowed us to obtain the raw data for both SIM6 and SIM9 in a single imaging session. SIM6 uses two phases (0, π), whereas SIM9 uses three phases (0, 2π/3, 4π/3) for reconstruction. As shown in Figs. S6a, b, both SIM6 and SIM9 achieved similar super-resolution results compared to WF imaging. To perform quantitative analysis, we also conducted SNR analysis and image decorrelation for SIM6 and SIM9, with results shown in Figs. S6c, d. The analysis indicates that SIM6 and SIM9 yielded comparable resolutions, demonstrating that our frame-reduction SIM is not inferior to SIM9 in terms of performance. Furthermore, SIM6 and SIM9 showed similar SNR values for both samples. Although SIM6 had a slightly lower SNR and resolution compared to SIM9, it can also generate high-fidelity super-resolution reconstruction with reduced data acquisition time and phototoxicity.

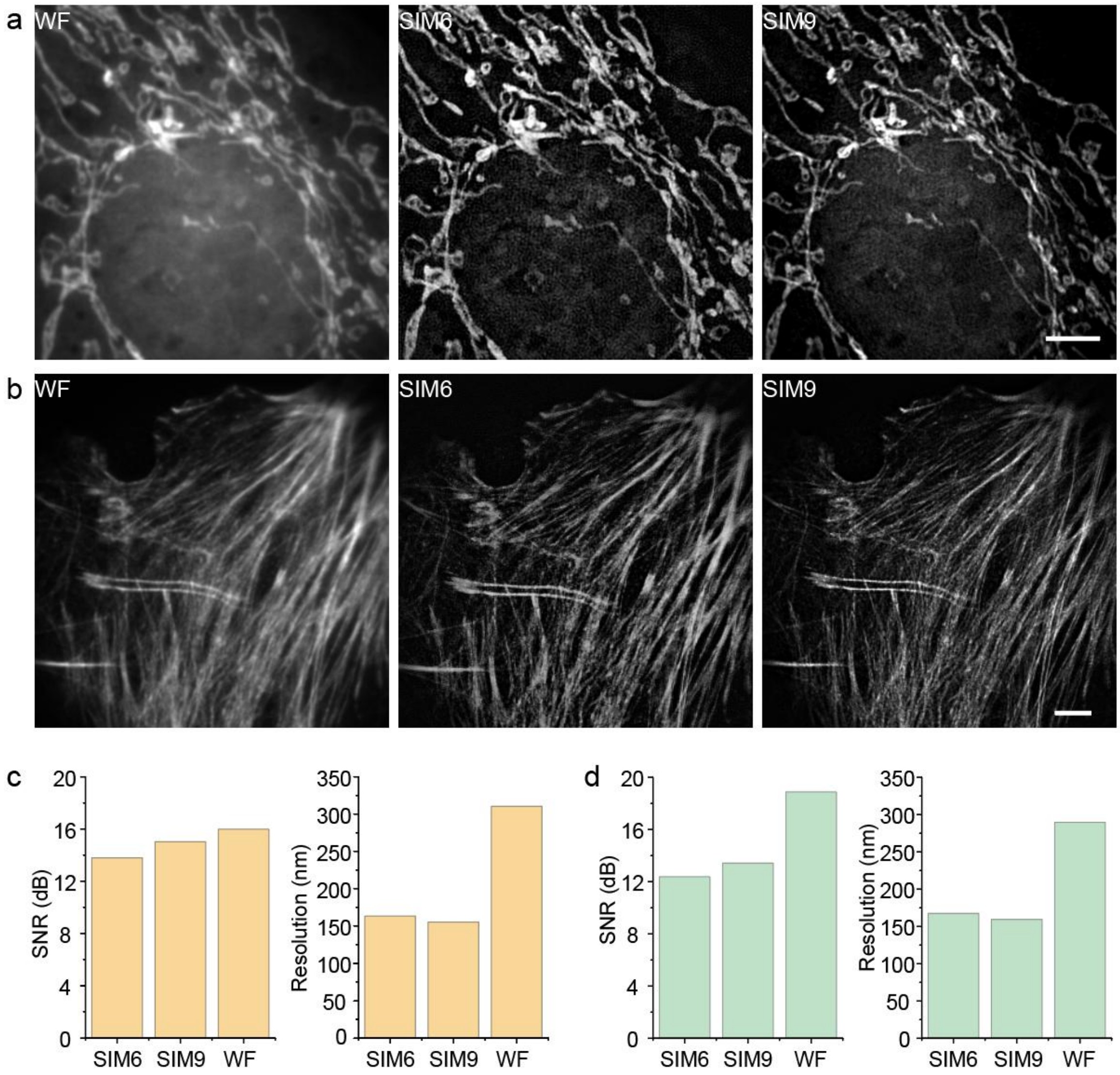

Fig. S6 Comparison of reconstruction results between SIM6 and SIM9. a. Comparison of WF, SIM6, and SIM9 images of mitochondria acquired by MFPM with a 100× objective. Scale bar: 4 μm. b. Comparison of WF, SIM6, and SIM9 images of actin filaments with a 100× objective. Scale bar: 4 μm. c. Quantitative comparison of SNR and resolution for different reconstruction results in the mitochondria sample. d. Quantitative comparison of SNR and resolution for different reconstruction results in the actin filament sample.

Additionally, to evaluate the effectiveness of our frame reduction algorithm in terms of illumination dose, we performed simulations on various structures, including line-shaped, point-shaped, and circle-shaped features. The results under different doses are shown in Fig. S7, with raw data SNRs of 42.3 dB, 26.6 dB, and 19.3 dB, respectively. It shows that as the SNR of raw data decreases, the quality of the reconstructed results degrades correspondingly, and the adjacent lines become unresolved and merged in noise. We further conduct the resolution analysis on those conditions. The resolution analysis shows that, although the resolution decreased as the SNR decreased, it remained relatively stable.

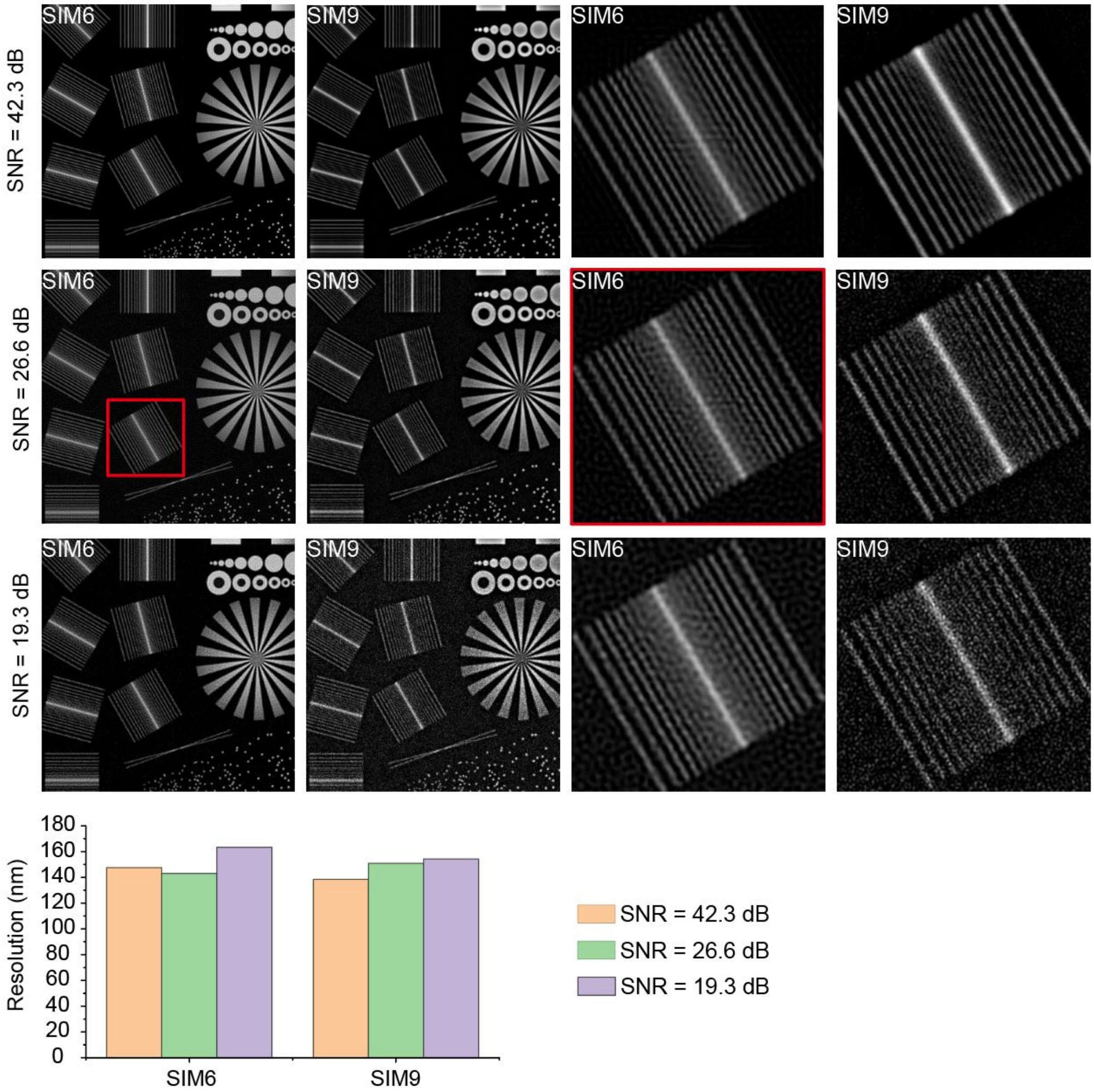

Fig. S7 Simulation-based evaluation of the frame-reduction reconstruction strategy. Representative line-, point-, and circle-shaped structures reconstructed using SIM9 and SIM6 under high-dose (top row, SNR = 42.3 dB), medium-dose (second row, SNR = 26.6 dB), and low-dose (third row, SNR = 19.3 dB) conditions. And the resolution comparison of SIM6 and SIM9 under different dose levels (last row).

We further compared SIM6 and SIM9 reconstructions using high- and low-SNR mitochondria images of 27.7 dB and 24.5 dB acquired with our MFPM system, as shown in Fig. S8. SIM6 closely matched the reconstruction quality of SIM9 under high-SNR conditions. Under low-SNR conditions, both SIM6 and SIM9 showed some degradation, but SIM6 still maintained effective detail recovery and super-resolution abilities, demonstrating the robustness and dose efficiency of the frame-reduction strategy. The resolution analysis also demonstrated that SIM6 remained stable resolution expansion compared with WF under low SNR.

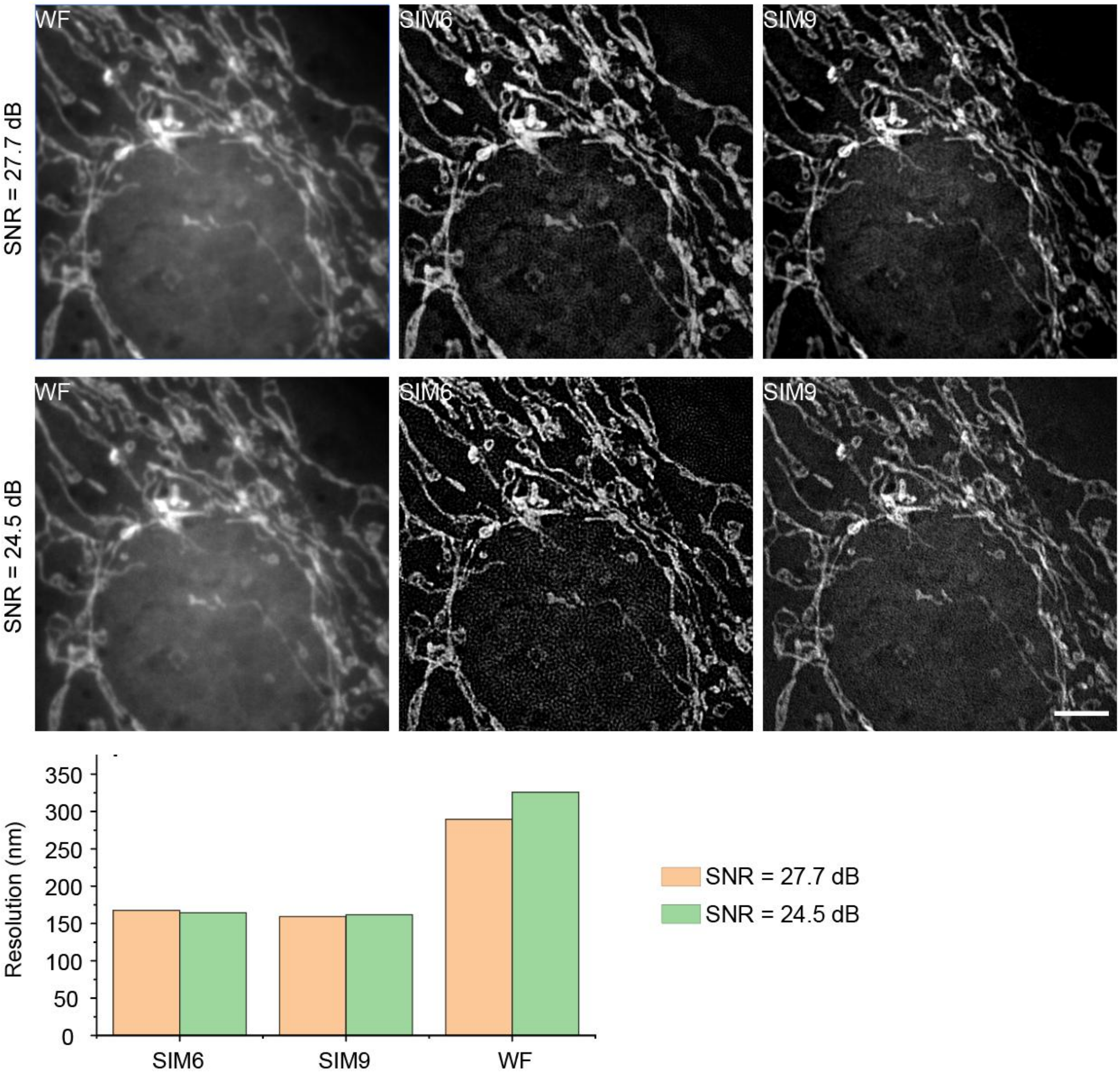

Fig. S8 Comparison of reconstruction results of SIM6 and SIM9 under high- and low-SNR conditions. Mitochondria images acquired on the MFPM system using a 100× objective. Top row: WF, SIM6, and SIM9 reconstructions at high dose (SNR = 27.7 dB). Second row: WF, SIM6, and SIM9 reconstructions at low dose (SNR = 24.5 dB). Bottom row: resolution comparison of SIM6 and SIM9 at different SNR levels. Scale bar: 4 μm.

Supplementary Note 6: Core parameter selection strategy

6.1 LED-array configuration

The LED array configuration, particularly the illumination numerical aperture σ and the illumination coherence parameter σ has a direct and substantial effect on the DPC imaging. Where σ is given by:

$$\sigma = \frac{NA_{illum}}{NA_{obj}} \tag{20}$$

To illustrate this point, we used simulations to detail the variations in the NA_{illum} (or σ) and the NA of the inner ring of the annular illumination NA_{in} (or $\sigma_{in} = NA_{in} / NA_{obj}$). The detailed results are as follows:

- **Role of σ**

Our phase transfer function (PTF) simulation results are shown in Fig. S9. Based on the information in the figure, we can draw the following conclusions.

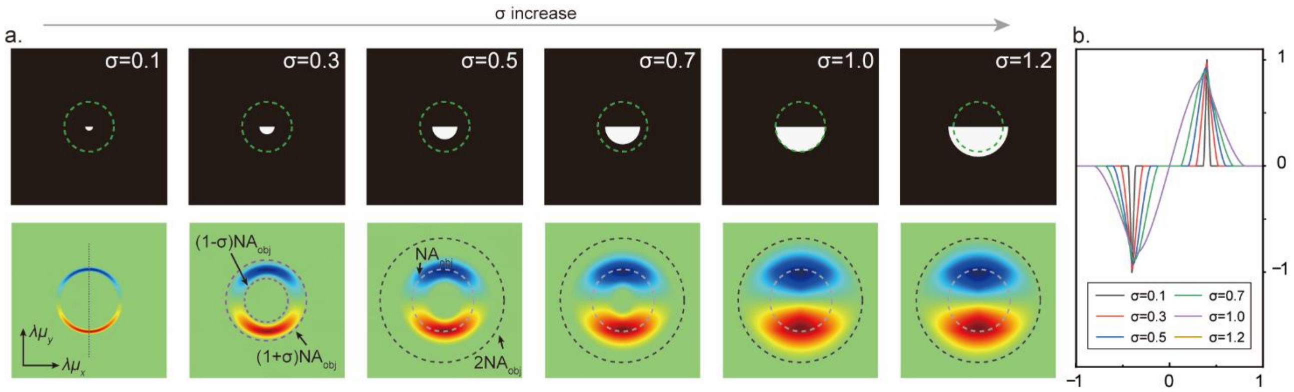

Fig. S9 **PTF and its central secant plot for different values of** σ **. a.** First row: the relationship between NA_{illum} (while half-circle) and NA_{obj} (green dashed line). Second row: the PTF corresponding to different values of σ . **b.** The central secant plot results of PTF corresponding to the black dotted line in a.

As shown in Fig. S9a and Equations (1-4) in Supplementary Information, it's clear that when $\sigma < 1$, the two shifted pupil functions exhibit a large overlapping region, leading to substantial cancellation in their difference. As a consequence, both low-frequency components below $(1-\sigma)NA_{obj}$ and high-frequency components above $(1+\sigma)NA_{obj}$ become partially missing, resulting in reduced phase contrast and incomplete frequency transfer. As σ increases, this overlapping region gradually diminishes, and the proportion of recoverable spatial-frequency information increases accordingly. When optimal condition occurs at $\sigma = 1$, where the two pupil functions become tangent. At this point, the overlap at low frequencies vanishes and the high-frequency coverage reaches its maximal extent, yielding the strongest and most balanced PTF response. As σ is increased to a value greater than 1, the range of PTF no longer expands. Furthermore, as shown in Fig. S9b, the central secant plot of the PTF completely coincides with the section when $\sigma = 1$.

Therefore, it is essential to ensure that the coherence factor of the illumination source equals or exceeds 1 in the experiment, which indicates that $NA_{illum} \geq NA_{obj}$. While NA_{illum} can be adjusted through two approaches: First, by varying the distance between the LED array and the sample while keeping the radius of the LED source constant. Second, by modifying the illumination radius of the LEDs while maintaining a fixed height between the LED array and the sample.

The latter method was adopted in this study, as it allows for precise control of NA_{illum} through programmable adjustments to the LED array, eliminating the need for mechanical movement and thereby enhancing operational efficiency and stability.

- **Influence of annular (semi-ring) LED illumination**

In addition to the coherence parameter σ ,we also analyzed the influence of annular (semi-ring) illumination generated by selecting LEDs with a non-zero inner numerical aperture σ_{in}. Simulation in Fig. S10a show that, converting a semi-circular illumination pattern into an annular one can narrowing the annulus reduces the overlap between the two shifted pupil functions. As shown in Fig. S10b, as σ increases, the central secant line becomes steeper, which corresponds to higher contrast in the image. Note that in experiment, when the intensity of individual LEDs is fixed, enlarging the NA_{in} leads to a reduction in the total optical power density, thereby requiring an increase in exposure time to maintain adequate signal levels. This trade-off necessitates careful optimization during experiments.

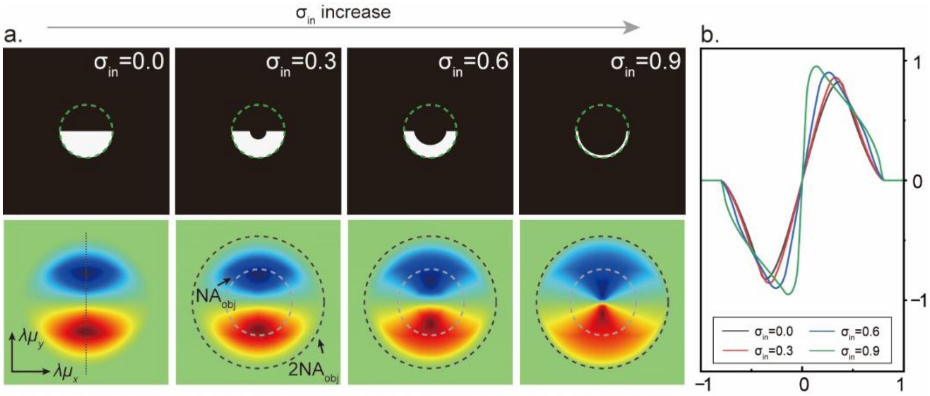

Fig. S10 PTF and its central secant plot for different values of σ_{in}. a. First row: change of NA_{in} while the illumination is semi-circular, with $NA_{illum} = 1$. Second row: corresponding PTFs for different values of σ_{in}. b. Central secant plots of the PTF, corresponding to the black dotted lines in a.

6.2 The regularization parameter in phase reconstruction

To clarify the impact of the regularization parameter in phase reconstruction, we reconstructed two sets of samples with different regularization parameters, and the reconstruction results are shown in Fig. S11. It can be observed that when the parameter setting is small, the SNR of the reconstructed image is low, and its noise resistance is weak. When the parameter setting is large, the image background is uniform, but the overall image is overly smoothed, leading to a smaller reconstructed phase value. We can also conclude that slight illumination non-uniformity in practical experiment can be mitigated by appropriately adjusting the regularization parameter, further demonstrating the robustness of the algorithm. Based on the existing literature and our experience from practical experiments[5, 6], we chose 5e-3 as the regularization parameter to strike a balance between noise reduction and image structure information recovery in this experiment. However, different samples may require different optimal optimization conditions, and the regularization parameter can be adjusted accordingly based on the specific characteristics of the sample.

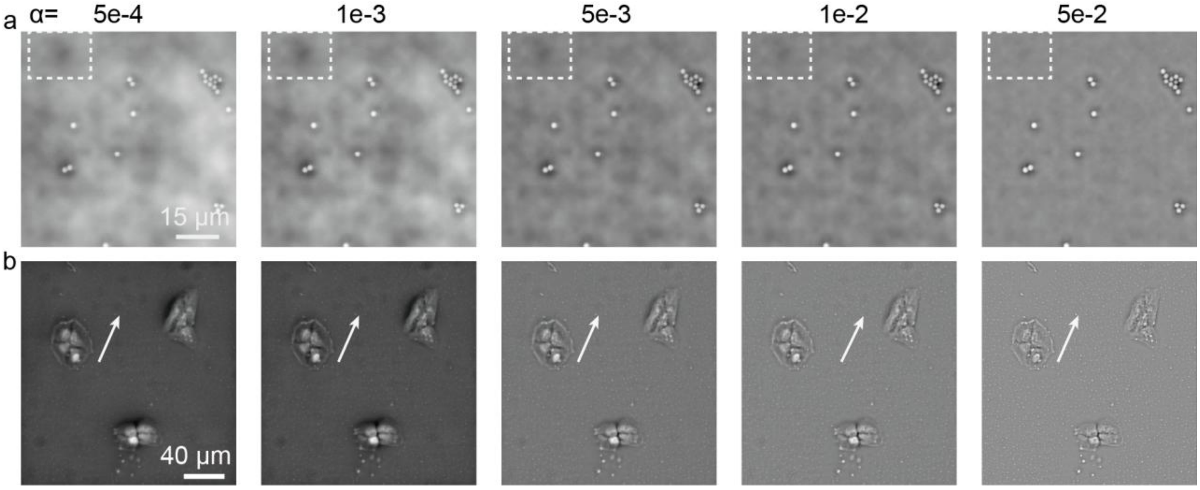

Fig. S11 The effect of different regularization parameters on the reconstruction results. a. Reconstruction results of fluorescent beads. From left to right, the regularization parameter increases, and the cloudy noise in the background within the white dashed boxes gradually decreases. b. Reconstruction results of U2OS cells. The background in the area indicated by the white arrows gradually becomes smoother.

6.3 Cutoff frequency and filtering window size of Dark Sectioning

In Dark sectioning, we first separate the frequency into high and low frequency domains, and only conduct the de-background on the low frequency. The high-frequency part is unchanged for the maintenance of weak information. We used different cutoff frequencies to conduct Dark sectioning in Fig. S12. It showed that when the cutoff frequency is lower, the weak information will be sacrificed, but the de-background capability will be increased. In the calculation, we set the cutoff frequency equal to 0.5 to balance the de-background and weak information maintenance.

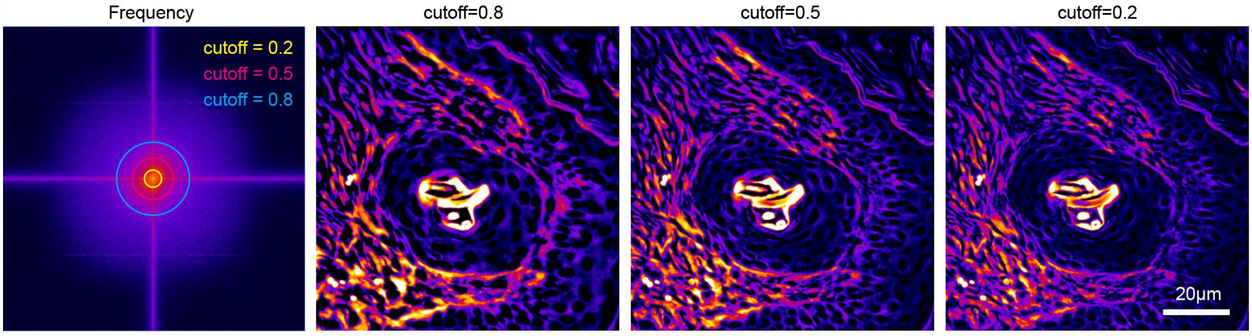

Fig. S12 Cutoff frequency in Dark sectioning. Left: schematic diagram of different cutoff frequencies. Right: influence of different cutoff frequencies on background suppression performance.

In addition to the cutoff frequency discussed above, the filtering window size used in the Dar sectioning background-removal step is equally important. In our implementation, the default block size is chosen to match the in-focus PSF, which is also the setting commonly adopted in 2D-SIM processing. As the thickness of the sample gradually increases, dark sectioning require adjustment to compensate for increased scattering or optical aberrations. To evaluate the sensitivity of dark sectioning to block size, we additionally tested a relatively thick tissue sample (~20 μm). Using the default block size of 16 pixels as a reference, we compared results across multiple settings. When the block size was reduced below the default value, the background removal became incomplete, leaving residual low-frequency components. Conversely, increasing the block size beyond the default caused the loss of fine structural details due to over-smoothing of weak signals. For this particular thick-tissue case, a block size of 9 pixels provided the best balance between suppressing defocused background and preserving structural information, as shown in Fig. S13.

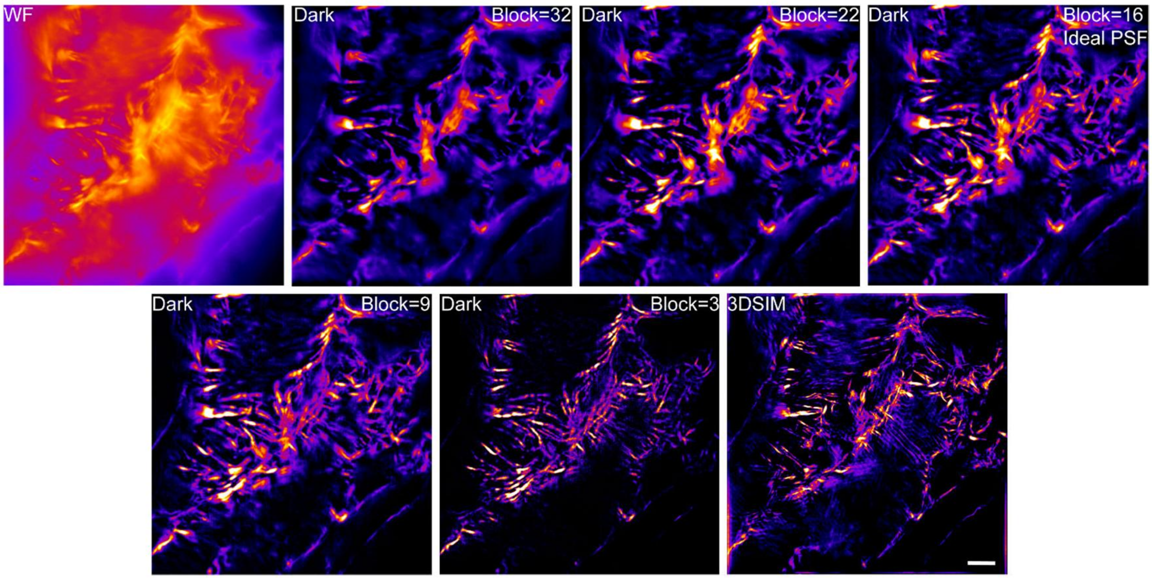

Fig. S13 **Dark sectioning results under different block sizes.** Top left: wide-field image. Bottom right: 3DSIM image. Intermediate panels: reconstruction results with gradually decreasing block size. Scale bar: 4 μm.

Supplementary Note 7: Multimodal imaging of mouse skin tissue sections

H&E stained mouse skin tissue sections were imaged using BF, DPC, and SR-SIM modes, as shown in Fig. S14a. Fluorescence images were merged with both BF and fDPC images, and the glandular region was further enlarged for detailed observation, as presented in Figs. S14b, c. The results indicate that both fDPC and BF modalities effectively revealed the overall structural contours of the sample, while fDPC additionally provided phase gradient information that was absent in the BF images, as highlighted by the arrow. Meanwhile, the fluorescence imaging results exhibited finer structural details, complementing the information obtained from the phase modes. This confirms the capability of the multimodal imaging system to capture complementary structural information. Additional regions of the tissue sections were also selected and imaged, the results are shown in Fig. S15a. Subsequently, the fluorescence intensity was compared under different imaging conditions. As shown in Fig. S15b, both OS-SIM and SR-SIM reconstruction results produce images with more distinct and resolvable structures and reduced background compared to WF images. Furthermore, the normalized intensity profile demonstrates that SR-SIM imaging achieves higher contrast than both OS-SIM and WF methods. Specifically, since the tissue sections employed in our experiments were 5 μm thick, they introduced only small amount out-of-focus background fluorescence. However, as imaging depth increases (e.g., to 25 μm), the SNR of WF images diminishes, consequently leading to a reduction in the SNR of the corresponding SR-SIM images. Notably, this depth already exceeds the typical imaging depth achievable with 2D-SIM. Therefore, effective background suppression is assisted by Dark sectioning in the SIM imaging, provided that the fringe pattern can adequately penetrate the sample to the desired depth.

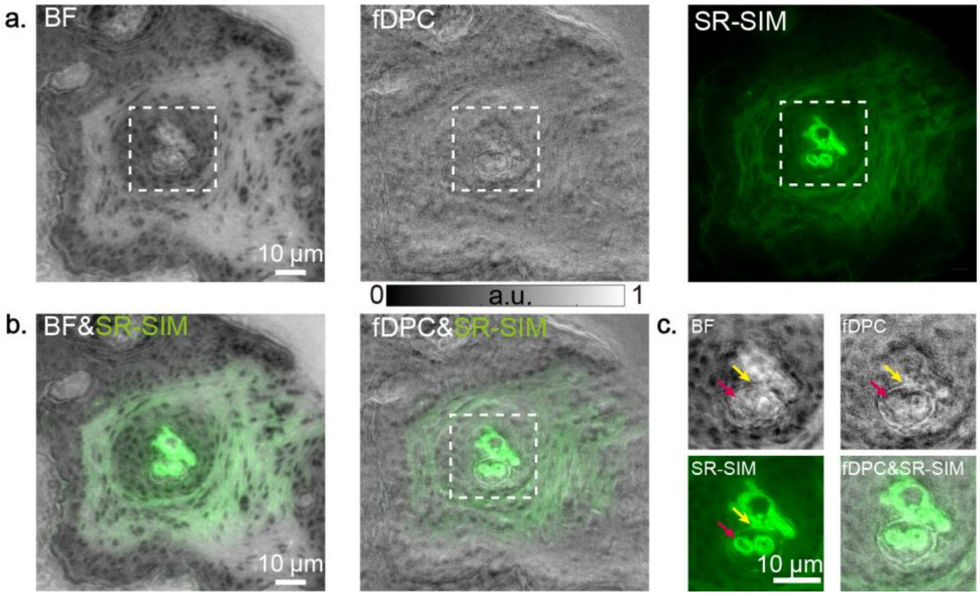

Fig. S14. Multimodal imaging results of H&E-stained mouse skin tissue sections. a. Imaging results of tissue sections using BF, fDPC, and background-removed SR-SIM modalities. **b.** Merged images of BF with SR-SIM, and fDPC with SR-SIM. **c.** Enlarged views of the regions indicated by the white dashed boxes in b.

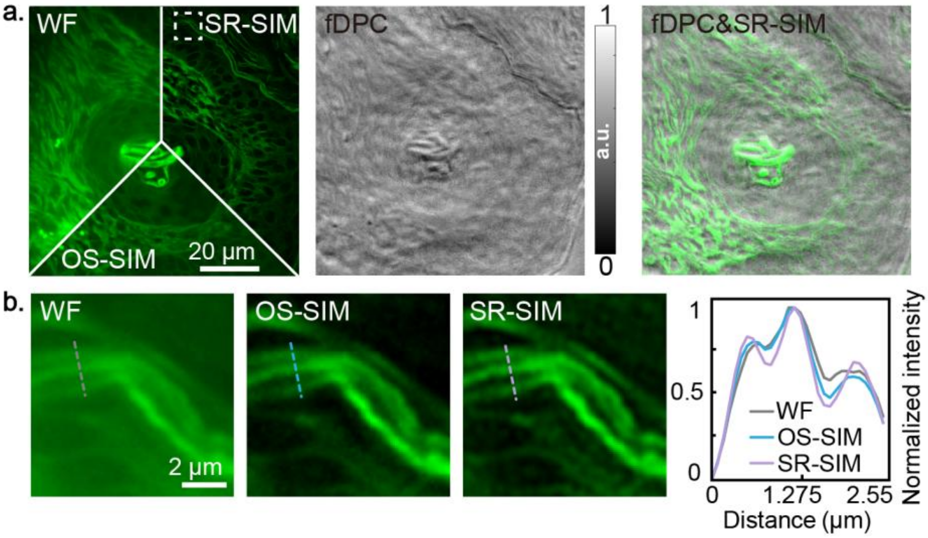

Fig. S15 **The comparison of multimodal imaging and fluorescence imaging of mouse skin tissue sections. a.** Fluorescence and fDPC images and merged results. **b.** Fluorescence images acquired under WF, OS-SIM, and SR-SIM modes, along with their corresponding normalized intensity profiles.

Supplementary Note 8: MFPM imaging of cell death dynamics

L929 cells exhibit strong proliferative and migratory capabilities under in vitro culture conditions and are highly sensitive to environment changes. When stimulated by chemical agents or external factors, these cells undergo typical apoptotic or necrotic processes, making them a widely used model for investigating cell death mechanisms[7, 8]. Moreover, as L929 cells typically adhere and grow in a monolayer configuration, they are particularly well-suited for long-term observation using DPC. Previous studies have utilized phase-contrast microscopy to monitor the apoptotic process induced by tumor necrosis factor (TNF), not only recording morphological changes in real time but also providing direct morphological evidence for distinguishing different types of cell death[9]. However, such methods rely primarily on visual interpretation to assess overall phase changes and are limited in their ability to reveal subtle structural alterations that occur during the cell death process.

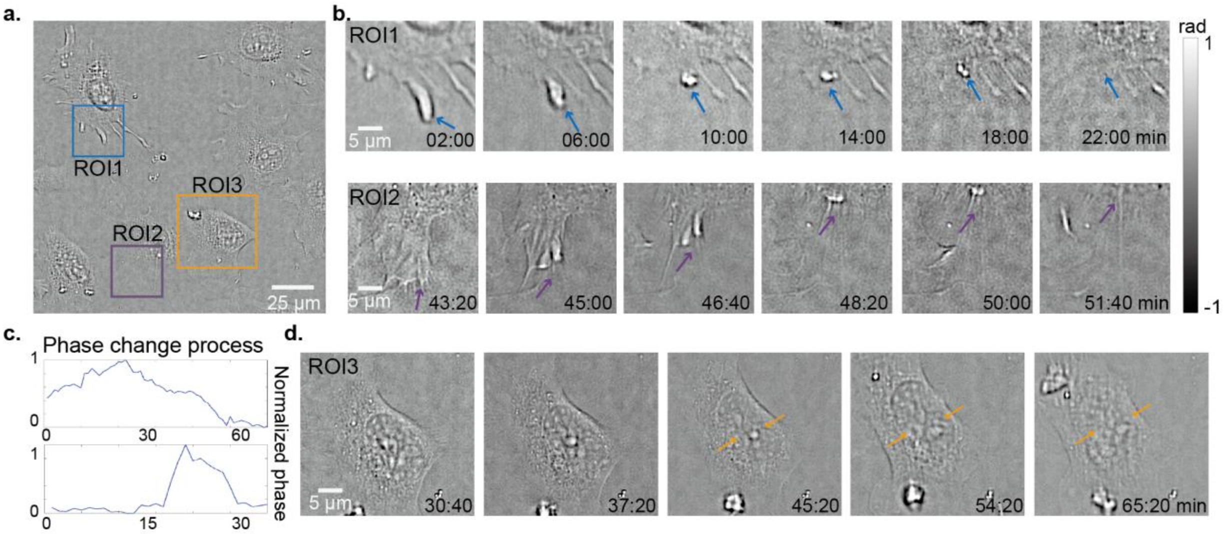

Fig. S16 DPC imaging of the cell death process in L929 cells. a. Reconstructed phase image at the initial time point. **b.** Enlarged view of the blue (ROI1) and purple-framed (ROI2) regions in a, with arrows indicating the trajectory of pseudopod movement, demonstrating its contraction process. **c.** Phase change curve corresponding to the pseudopod contraction process in b. **d.** Enlarged view of the orange-framed region in a, with arrows indicating the morphological changes of the cell nucleus during cell division.

To this end, we employed qDPC imaging to perform local dynamic observations (1024 pixel × 1024 pixel) of L929 cells. During the experiment, a set of data was acquired every 20 s for reconstruction, continuously recording the dynamic process of cell death for over 2 h. As shown in Fig. S16a, the reconstructed phase image at the initial time point reveals the overall morphology and quantitative phase distribution of L929 cells under a large FOV. Under the culture conditions of

37 °C and 5% carbon dioxide, L929 cells initially exhibited a well-spread morphology. However, as the cells gradually deviated from the optimal growth condition, morphological changes began to emerge. The earliest observable change was the contraction of cellular pseudopodia, as illustrated in Figs. S14a, b. The pseudopodia gradually curled up from their initial adherent state, resulting in an increase in thickness in localized region, which manifested as a gradual increase in recovered phase values. As time passes, the pseudopodia continued to contract until they completely disappear, with the corresponding phase values returning to baseline. We statistically analyzed the phase changes during pseudopod contraction process and plotted the temporal evolution of quantitative phase values over sequential frames, as shown in Fig. S16c, enabling quantitative analysis of the dynamic evolution of pseudopods.

Additionally, we captured the mitotic process of L929 cells, as presented in Fig. S16d. The time-lapse sequence reveals gradual disintegration of the nuclear envelope and the elongation of the cell nucleus. These observations demonstrate the potential of qDPC imaging for capturing the dynamic morphological features of cell division processes.

Supplementary Note 9: Sample Preparation

9.1 Preparation of fluorescent beads samples

Prior to sample preparation, the coverslips were pretreated by immersion in the poly-L-lysine solution (poly-L-lysine: ultrapure water: balanced salt solution = 3:1:1) for 1 hour. The coverslips were then rinsed 2–3 times with ultrapure water and air-dried until no visible moisture remained. Then, the fluorescent microsphere stock solution (1 mL) was ultrasonicated to ensure thorough dispersion, and 1 μL of the stock was extracted and diluted to an appropriate concentration, followed by gentle mixing. Next, 100 μL of the diluted microsphere solution was dropped onto the pretreated coverslip and incubated in the dark for 30 minutes to allow particle attachment. The excess liquid was then removed, and the sample was gently rinsed twice with ultrapure water and air-dried. For mounting, a drop of ProLong antifade reagent was applied to the center of a clean microscope slide, and the coverslip was carefully placed on top, taking care to avoid air bubbles. The slide was stored overnight at 4 °C and sealed the following day using a commercially available sealant, completing the fluorescent microsphere sample preparation.

9.2 Preparation of zebrafish samples

In this study, red neutrophil Tg (lyzC:Cherry) transgenic zebrafish were used as the experimental model. Zebrafish embryos were incubated in E3 embryo medium at a constant temperature of 28 °C. During embryonic development, 1-phenyl-2-thiourea (PTU) was added to inhibit melanin formation, thereby maintaining the transparency of the larvae for subsequent imaging. After 1–2 days of incubation, larvae were anesthetized using a suitable concentration of ethyl 3-aminobenzoate methane sulfonate to facilitate immobilization. The anesthetized larvae were then embedded in low-melting-point agarose before solidification, and the orientation was quickly adjusted to a lateral position. Once the agarose had fully solidified, the larvae were transferred to a 35 mm glass-bottom dish for imaging, with E3 medium added to maintain viability. After imaging, the agarose was carefully removed and the larvae were returned to the embryo medium.

Supplementary Tables

Table S2. Comparison of existing polarization fluorescence microscopy

Techniques	Frames	Super-resolution	Optical-sectioning
SPOT[10]	6	No	Yes
pSIM[11]	9	Yes	No
MFPM	6	Yes	Yes

Supplementary Figures

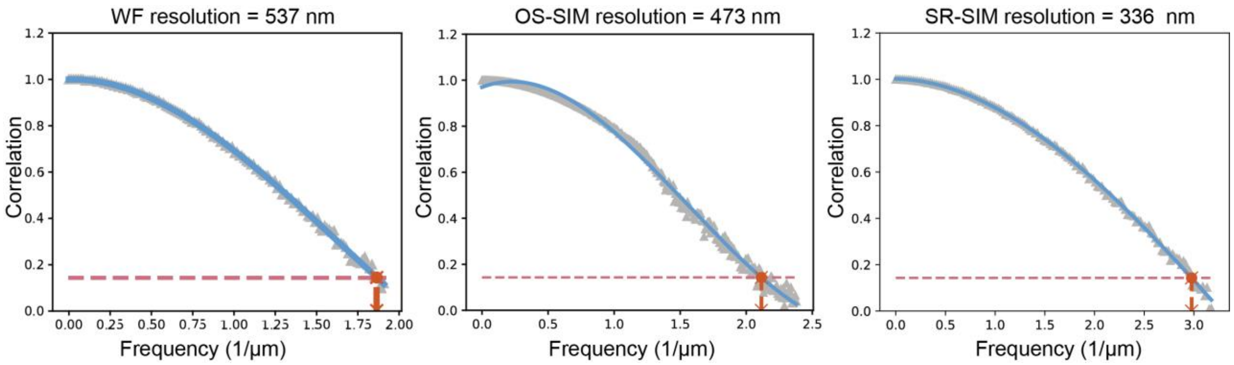

Fig. S17 **Fourier ring correlation analysis of three modes of the actin filament.**

Reference

1. Fan, Y. et al. Accurate quantitative phase imaging by differential phase contrast with partially coherent illumination: beyond weak object approximation. *Photonics Research* **11**, 442-455 (2023).
2. Wen, G. et al. High-fidelity structured illumination microscopy by point-spread-function engineering. *Light: Science & Applications* **10**, 70 (2021).
3. Müller, M. et al. Open-source image reconstruction of super-resolution structured illumination microscopy data in ImageJ. *Nature Communications* **7**, 10980 (2016).
4. Mo, Y. et al. Quantitative structured illumination microscopy via a physical model-based background filtering algorithm reveals actin dynamics. *Nature Communications* **14**, 3089 (2023).
5. Tian, L. & Waller, L. Quantitative differential phase contrast imaging in an LED array microscope. *Optics Express* **23**, 11394-11403 (2015).
6. Chen, M., Phillips, Z.F. & Waller, L. Quantitative differential phase contrast (DPC) microscopy with computational aberration correction. *Optics Express, Vol. 26, Issue 25, pp. 32888-32899* (2018).
7. Vanlangenakker, N. et al. TNF-induced necroptosis in L929 cells is tightly regulated by multiple TNFR1 complex I and II members. *Cell Death & Disease* **2**, e230-e230 (2011).
8. Kearney, C.J. et al. Necroptosis suppresses inflammation via termination of TNF- or LPS-induced cytokine and chemokine production. *Cell Death & Differentiation* **22**, 1313-1327 (2015).
9. Sawai, H. Induction of apoptosis in TNF-treated L929 cells in the presence of necrostatin-1. *International Journal of Molecular Sciences* **17**, 1678 (2016).
10. Zhanghao, K. et al. High-dimensional super-resolution imaging reveals heterogeneity and dynamics of subcellular lipid membranes. *Nature Communications* **11**, 5890 (2020).
11. Zhanghao, K. et al. Super-resolution imaging of fluorescent dipoles via polarized structured illumination microscopy. *Nature Communications* **10**, 4694 (2019).